Journal of Physics and Chemistry of Solids 175 (2023) 111202

Contents lists available at ScienceDirect

Journal of Physics and Chemistry of Solids

journal homepage: www.elsevier.com/locate/jpcs

Pressure-induced valence fluctuation in $CsEuF_3$: From divalent Eu valence to trivalent Eu valence state

Takeshi Nakagawa [a,*], Martina Vrankić [b], Melita Menelaou [c], Raimundas Sereika [a,d], Dong Wang [a], Jianbo Zhang [a], Hirofumi Ishii [e], Nozomu Hiraoka [e], Yang Ding [a,**]

[a] Center for High Pressure Science and Technology Advanced Research, 10 Xibeiwang East Road, Haidian District, Beijing, 100094, PR China
[b] Division of Materials Physics and Center of Excellence for Advanced Materials and Sensing Devices, Ruđer Bošković Institute, Bijenička 54, 10000, Zagreb, Croatia
[c] Department of Chemical Engineering, Cyprus University of Technology, Limassol, 3036, Cyprus
[d] Vytautas Magnus University, K. Donelaičio Str. 58, LT-44248, Kaunas, Lithuania
[e] National Synchrotron Radiation Research Center, Hsinchu, 30076, Taiwan

ARTICLE INFO

Keywords:
Perovskites
Rare-earth elements
Valence fluctuation
Synchrotron X-ray absorption spectroscopy
High pressure

ABSTRACT

The ternary rare-earth metal fluoride $CsEuF_3$ adopts an ideal cubic perovskite structure [ABX_3] under ambient conditions. The B-cation site is occupied by the rare-earth Eu ion and EuF_6 octahedra are formed. In the present study, magnetic susceptibility and synchrotron X-ray absorption spectroscopy (XAS) analysis at the Eu-L_3 edge confirmed that Eu is in a divalent oxidation state under ambient conditions. Temperature-dependent magnetic susceptibility data revealed that the average Eu valence increased below 20 K due to a partial transition from the Eu^{2+} state to the Eu^{3+} state, thereby resulting in a mixed valence state with an average valence of +2.23. Direct evidence for valence fluctuation by the Eu ions in $CsEuF_3$ was obtained using the high pressure high energy resolution fluorescence detection-XAS technique, where continuous changes in valence were observed from 2.15+ at ambient pressure up to 2.5+ at 10.5 GPa. These findings indicate the possibility of discovering interesting physical properties associated with valence instabilities by rare-earth metals in similar systems.

1. Introduction

The highly correlated narrow-band behavior of 4f electrons in rare-earth (RE) systems has attracted considerable interest recently, and it is referred to as one of the "key ingredients for modern technology." The variable valence states and electronic structures with flexible redox properties of these systems lead to interesting exotic behaviors, including volume collapse, Kondo-like behavior, high magnetic ordering temperature, and heavy fermion behavior [1–5]. These elements have traditionally been used as dopants to modify the specific physical and chemical properties of a wide range of materials. For instance, several studies have shown that the introduction of RE metals as dopants or components of RE-containing perovskite materials can significantly improve the performance of perovskite solar cells, the photoluminescence of perovskite and/or double perovskite nanocrystals, and the efficiency of perovskite catalysts [6–11].

In addition, materials with a perovskite crystal structure have been studied intensively because they exhibit several features that are important for technical and fundamental reasons [12–14]. The earliest identified perovskite is $CaTiO_3$. Subsequently, this formula was derived into new different forms, including ABX_3, $A_3B_2X_9$, and A_4BX_6, where A and B are cations (A has a larger radius than B), and X is either a halogen anion or oxygen anion. Moreover, these materials can exhibit emergent physical properties as well as various electronic, magnetic, and structural behaviors, which are strongly associated with the cation that occupies the A- and/or B-site, and their versatile spatial arrangement in BX_6 octahedra [15]. Therefore, these diverse compositions and structures make perovskite materials important as functional materials with a wide range of applications, including in luminescent perovskites used in sensors, photoelectric perovskites used in photovoltaics, electrical perovskites used to prepare devices, and magnetic perovskites used in biomedical imaging and other fields. Many elements can occupy the cation site but few studies have investigated RE-based perovskite materials, i.e., materials where RE metals occupy the B-site to form BX_6 octahedra, and we lack an understanding of their physical properties.

Thus, in the present study, we synthesized the material $CsEuF_3$ using

* Corresponding author.
** Corresponding author.
E-mail addresses: takeshi.nakagawa@hpstar.ac.cn (T. Nakagawa), yang.ding@hpstar.ac.cn (Y. Ding).

https://doi.org/10.1016/j.jpcs.2022.111202
Received 1 March 2022; Received in revised form 25 December 2022; Accepted 26 December 2022
Available online 27 December 2022

the chemical reduction route [16] in order to understand the fundamental properties of RE-based perovskite materials, and by focusing on cases where the divalent RE ion forms octahedra. $CsEuF_3$ is a rare example in this class of materials because it contains a divalent Eu ion in the B-site and forms an ideal cubic perovskite structure under ambient conditions (Fig. 1). In previous studies, $CsRECl_3$ (where RE = Sm, Eu, Tm, Yb), $CsREF_3$ (where RE = Eu, Yb), and $CsEuBr_3$ were successfully synthesized and their reported crystal structures contain divalent REs that form BX_6 octahedra [16–18].

Typically, RE chemistry is dominated by the trivalent oxidation states, but elements such as cerium, praseodymium, and terbium exhibit an additional tetravalent oxidation state, and samarium, europium, and ytterbium have an additional divalent oxidation state [19–21]. The physical properties of Eu are significantly different in these two oxidation states, where Eu^{2+} ($[Xe]4f^7$) has high magnetic moments ($J = 7/2$) compared with nonmagnetic Eu^{3+} ($[Xe]4f^6$) ($J = 0$). Furthermore, a small energy difference between the $4f^7$ and $4f^6$ states of Eu^{2+} and Eu^{3+}, respectively, can lead to valence instability in response to changes in external stimuli, such as temperature or pressure (chemical or physical). The valence state of the RE ion can be determined by subtle differences in the interaction energy between localized *f* electrons and the cohesive energy of electrons populating the conduction bands in the metal [22], which can be observed by using various macroscopic and microscopic experimental techniques.

The isolated $CsEuF_3$ compound was characterized based on powder X-ray diffraction (PXRD), temperature-dependent magnetic susceptibility measurements, and high energy resolution fluorescence detection-X-ray absorption spectroscopy (HERFD-XAS) under applied pressure. Our results indicated that the $CsEuF_3$ compound was characterized by a fluctuating valence system where 50% of the divalent Eu ions transformed into the trivalent oxidation state as the pressure increased.

2. Materials and methods

Synthesis: A polycrystalline sample of the fluoroperovskite analogue $CsEuF_3$ was synthesized via the chemical reduction of europium trifluoride (EuF_3, Alfa Aesar, 99.98%) with cesium metal (Cs, Alfa Aesar, 99.98%). Stoichiometric amounts of EuF_3 and Cs metal were placed in a tantalum tube and sealed under reduced pressure inside a quartz tube. The mixture was annealed at 723 K for 24 h and then ground into powder. All sample handling procedures were conducted in an argon-filled glove box under anaerobic conditions (O_2/H_2O values < 0.1 ppm) because the materials are sensitive to oxygen and moisture.

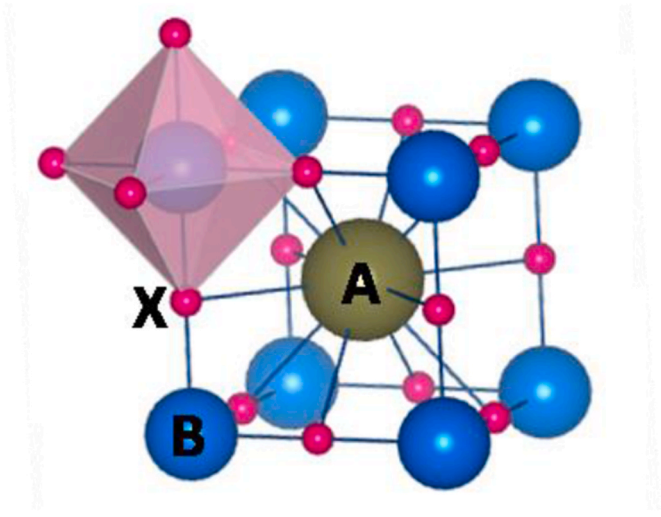

Fig. 1. Schematic illustration of ABX_3 cubic perovskite, where the A and B cation sites, and X anions occupy the body-centered, vertices, and face-centered positions, respectively (A = Cs; B = Eu; X = F). The RE metal ion occupies the B-site to form BX_6 octahedra.

PXRD: The sample was sealed in a thin-walled glass capillary with a diameter of 0.5 mm to perform PXRD measurements under ambient conditions. PXRD measurements were acquired using a Rigaku SmartLab-9kW equipped with a Mo-target X-ray tube ($\lambda = 0.7093$ Å) and D/teX Ultra-HE detector. The glass capillary was continuously rotated at 60 rpm. Data were obtained in the 2θ range of 5–60° at a step interval of 0.005°.

Quantitative phase analysis was performed using Rietveld structure refinement [23] and according to the guidelines of Hill and Howard [24]. Structure refinements using PXRD data were conducted using GSAS2 software [25]. The starting models for the $CsEuF_3$, CsF, and EuF_3 phases were based on those described by Wu and Hoppe [16] (ICSD card no. 49577), Posnjak and Wickoff [26] (ICSD card no. 53832), and Zinchenko et al. [27] (ICSD card no. 53832), respectively. According to the instrumental parameters (such as the sample displacement and scaling factor), lattice parameters, and peak shape parameters for all of the phases present, structural refinement was performed using a pseudo-Voigt profile function and a Chebyschev-1 background model with up to three coefficients. Isotropic vibration modes were assumed for all atoms. In particular, the fluoride isotropic displacement parameter was maintained at a reasonable value ($U_{iso} = 0.066(2)$ Å^2) with a minimal impact on the reliability factor, whereas the isotropic displacement parameters for Cs and Eu in the $CsEuF_3$ phase were allowed to be modified freely.

Magnetic susceptibility: Magnetic measurements were performed for a sample weighing ~20 mg sealed in a thin-walled quartz ampoule using a Quantum Design SQUID MPMS magnetometer. Temperature-dependent magnetic susceptibility data were collected at 1 T under field-cooled protocols at temperatures between 1.8 and 300 K. Magnetic susceptibility was calculated based on the zero-field cooled magnetization measurements. The inverse magnetic susceptibility was fitted to the modified Curie–Weiss law as follows:

$$\chi_p(T) = \frac{N_A}{3k}\frac{\mu_{\mathrm{eff}}^2}{T-\Theta_p} - \chi_D$$

where μ_{eff} is the effective magnetic moment, Θ_p is the paramagnetic Weiss temperature, and x_D is the diamagnetic contribution to the magnetic susceptibility. x_D is -75.9×10^{-9} emu/mol for $CsEuF_3$.

HERFD-XAS: Eu-L_3 edge XAS spectra were collected in the HERFD mode using the Taiwan inelastic X-ray scattering undulator installed in the BL12XU at SPring-8 (Hyogo, Japan). A monochromatic X-ray beam was produced using a Si(111) double crystal monochromator and the beam was focused with two Kirkpatrick–Baez mirrors to 8×45 μm^2 at the sample position. Measurements were made at ambient conditions using the same batch of samples enclosed inside the thin-walled glass capillary applied for PXRD analysis. The X-ray emissions from the sample were collected at an angle of 90° from the incident X-ray and analyzed using a spectrometer equipped with a spherically bent Ge(444) crystal (radius = 1 m) and a solid-state detector (XFlash 1001 type 1201) arranged in a horizontal plane in a Rowland-circle geometry. In the HERFD-XAS measurements, the intensity of the Eu-$L_{\alpha 1}$ fluorescence line was measured as a function of the incident photon energy, which varied around the Eu-L_3 absorption edge (6.9769 keV). The sample was aligned to minimize self-absorption and the acquisition time for each measurement was minimized to avoid radiation damage to the sample. A Panoramic-style DAC equipped with a 300 μm culet diameter anvil and a beryllium + cubic boron nitride gasket was used to apply high pressure. The $CsEuF_3$ powder samples were pressed into small pellets (thickness = 20 μm, area = 70×90 μm^2) and loaded together with a ruby ball and Daphne oil as a pressure transmitting medium.

Synchrotron PXRD: High pressure synchrotron PXRD measurements were performed at room temperature using the BL12B2 at SPring-8 (Hyogo, Japan). Two four-post wide-opening DACs with diamond anvils and a 300 μm culet diameter were used to apply pressure. The

powder samples were pressed into two small pellets (~70 × 90 μm^2) and loaded together with a ruby ball into a stainless-steel gasket hole. Daphne oil was used as a pressure transmitting medium and each pressure point was determined by the fitting pressure shift of the ruby fluorescence line. A monochromatic X-ray beam with a wavelength of 0.5657 Å was used as the probing source. The pressure was increased up to 23 GPa and released down to ambient pressure. Five relatively quick scans were acquired and summed in order to avoid the possibility of radiation damage to the sample and to improve the signal-to-noise ratio. The two-dimensional diffraction images were integrated using IPAnalyzer, and data analysis was performed by Rietveld refinement and the LeBail pattern decomposition technique in the GSAS2 suite of programs.

3. Results

3.1. PXRD measurements

As shown in Fig. 2, qualitative phase analysis indicated the formation of the major $CsEuF_3$ phase (wt.% fraction 96.8%) and two minor phases comprising CsF (wt.% fraction 1.9) and EuF_3 (wt.% fraction 1.3). Rietveld refinement of the PXRD pattern obtained for the sample collected under ambient conditions confirmed that $CsEuF_3$ adopts an ideal cubic perovskite structure (space group *Pm-3m*) with a lattice constant of a = 4.77776(3) Å and a total volume of V = 109.062(3) Å^3 (R_{wp} = 4.78%), which are consistent with previously published data [16]. The refined structural parameters for the $CsEuF_3$ phase are listed in Table 1. Eu ions fill the octahedral holes created by the F ions, and the Cs and F ions form a cubic closed packed lattice. The Cs atoms are in Wyckoff position 1*b*, ½,½,½; the Eu atoms are in Wyckoff position 1*a*, 0,0,0; and the F atoms are in Wyckoff position 3*d* ½,0,0; all of which are special positions. Together the atoms form a three-dimensional net of corner-sharing EuF_6 octahedra with Cs ions in the twelve-fold voids between the polyhedrons.

3.2. Magnetic property measurements

Temperature-dependent magnetic susceptibility measurements were obtained between 1.8 K and 300 K to determine the temperature dependence of the valence of Eu ions in $CsEuF_3$. Fig. 3 shows the temperature dependence of the paramagnetic susceptibility, χ, for $CsEuF_3$. At high temperatures, χ(T) followed the Curie–Weiss law with a positive

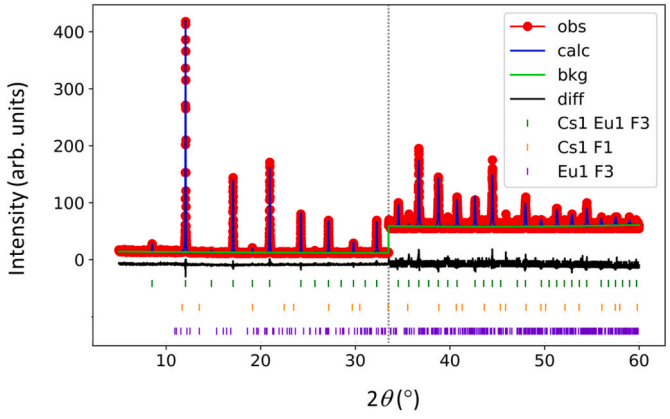

Fig. 2. Final X-ray diffraction profile (λ = 0.7093 Å) obtained for the $CsEuF_3$ sample at ambient conditions, i.e., red circles show the observed results and the solid blue line show those calculated by Rietveld refinement. The difference profile is represented by the lower black solid line, and the dark green, orange, and purple tick marks denote the reflection positions of the $CsEuF_3$, CsF, and EuF_3 phases, respectively. The lower solid green line represents the fitted background contribution. For clarity, the diffraction pattern from 2θ = 33° to 60° is shown enlarged five times.

Table 1
Summary of structure refinements obtained for $CsEuF_3$ by Rietveld refinement based on high quality laboratory PXRD data collected at room temperature (λ = 0.7093 Å). Estimated errors in the last digits are given in parentheses.

Atom	x	y	z	U_{iso} (Å^2)	Occupancy
Cs	0.5	0.5	0.5	0.0036(9)	1.0
Eu	0	0	0	0.0192(9)	1.0
F	0.5	0	0	0.066(2)	1.0

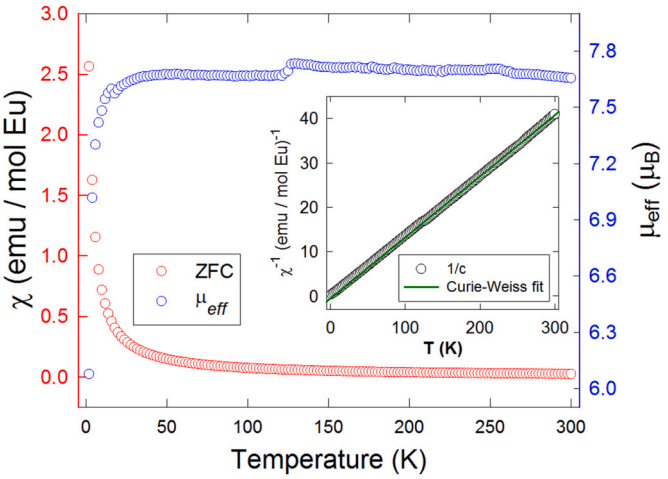

Fig. 3. Temperature dependence of the molar magnetic moment determined for $CsEuF_3$ after subtracting the diamagnetic core contributions from the difference in the values measured under magnetic fields of 4 and 2 T (left axis), and the effective magnetic moment of Eu^{2+} (right axis). The inset shows the inverse magnetic susceptibilities.

Weiss temperature (3.75 K), but the susceptibility increased sharply below 25 K to reach χ = 2.5 emu mol^{-1} at 1.8 K. The inverse susceptibility curve above 25 K was fitted with the Curie–Weiss law. The effective magnetic moment per Eu atom (μ_{eff}) at 300 K was determined as 7.62 μ_B and the Weiss temperature as Θ_p = 3.8 K. This value is slightly lower than the spin-only magnetic moment calculated for Eu^{2+} (7.94 μ_B/Eu atom), thereby indicating that Eu essentially existed as Eu^{2+}, i.e., 96% in the divalent state.

To understand the behavior of $CsEuF_3$ below 20 K, the temperature-dependent effective magnetic moment per Eu atom was calculated using the following formula:

$$(\mu_{eff})^2 = 8\ \chi\ T,$$

and the results are shown in the inset in Fig. 3. The effective magnetic moment remain unchanged down to 20 K, but a rapid decrease started at 18 K and μ_{eff} = 6.07 μ_B was reached at 1.8 K. This sharp decrease in the effective magnetic moment can be explained by the valence fluctuation model, where $CsEuF_3$ only contained paramagnetic Eu^{2+} ($4f^7$) at high temperature, but a spontaneous change in valence to nonmagnetic Eu^{3+} ($4f^6$) occurred as the temperature decreased. At the lowest temperature, 76% of the Eu ions were expected to be in the divalent state, and 24% changed to the trivalent state. Thus, the average valence of the Eu ions present in $CsEuF_3$ was +2.23. It should be noted that the effective magnetic moment of Eu was estimated based on the assumption that the Curie–Weiss law was valid down to the lowest temperature because an obvious deviation from the Curie–Weiss fit was not observed, even at 1.8 K. Direct experimental measurements, such as XAS, hard X-ray photoelectron spectroscopy, and Mössbauer spectroscopy, are required to confirm this transition. Nevertheless, the average valence of the Eu ions estimated in this study may not have reached the maximum conversion of divalent Eu ions.

3.3. XAS features

The valence states of Eu ions at ambient conditions can be directly extracted by using element-specific, bulk-sensitive spectroscopic techniques such as XAS. Thus, HERFD-XAS measurement at the Eu-L_3 absorption edge was conducted to estimate the valence state of the Eu ions in the EuF_3 and $CsEuF_3$ compounds at ambient conditions. Compared with conventional XAS, the resolution of the spectrum obtained by the HERFD-XAS mode is significantly improved, so even small energy differences between two different valence states can be detected [28]. The corresponding HERFD-XAS spectra for EuF_3 and $CsEuF_3$ are shown in Fig. 4. The spectrum for EuF_3 was first measured as a reference and it contained a strong peak at 6982 eV, which was attributed to the presence of the Eu^{3+} state (electronic configuration: $2p^63d^{10}4f^6 \rightarrow 2p^53d^{10}4f^65d^1 \rightarrow 2p^63d^94f^65d^1$). The spectrum for $CsEuF_3$ contained two peaks comprising one with higher intensity at 6975 eV for the Eu^{2+} state ($2p^63d^{10}4f^7 \rightarrow 2p^53d^{10}4f^75d^1 \rightarrow 2p^63d^94f^75d^1$) and a small Eu^{3+} peak at 6982 eV.

The small Eu^{3+} peak was potentially caused by the presence of contaminants, such as residual EuF_3 in the test powder sample, partial oxidation of the sample during sample preparation for tests, and partial oxidation caused by the incident beam during measurement. As expected, the Eu^{3+} peak rapidly increased when the X-ray beam was irradiated without filters and the Eu^{2+} peak was lost. In order to prevent radiation damage to the sample during the measurements, thick aluminum foil filters were added to reduce the incident X-ray beam power to the point that damage was no longer induced. As a consequence, signal-to-noise ratio loss occurred compared with that for the EuF_3 spectrum, but the good statistics still allowed us to follow the evolution of the average europium valence under pressure with sufficient accuracy.

Fig. 5 shows the spectra based on HERFD-XAS measurements at the Eu-L_3 absorption edge for $CsEuF_3$ at various pressures. At low pressures, the intensity of the Eu^{2+} peak was higher relative to that for Eu^{3+}. However, as the pressure increased, the intensity of the Eu^{3+} peak increased whereas that of the Eu^{2+} peak decreased. These qualitative findings indicate that the average Eu valence increased from +2 toward +3. Thus, in order to determine the average valence of the Eu ions in the $CsEuF_3$ at each pressure point and to obtain quantitative information about the pressure dependence, the HERFD-XAS spectrum was fitted with a two-component model consisting of an arctangent step function and a Lorentzian peak for each valence state. In particular, each component was fitted by the sum of an arctangent continuum excitation background and three Voigt functions (one main function and two satellites) to satisfactorily reproduce the white peaks.

The average Eu valence under ambient conditions was derived from the relative intensities of the divalent and trivalent peaks using the following simple formula [29]:

$$v = 2 + I(3+)/[I(2+)+I(3+)]$$

where $I(2+)$ and $I(3+)$ are the integrated intensities of the white XAS peaks assigned to Eu^{2+} and Eu^{3+}, respectively. In total, $I(2+) = 15.9$ and $I(3+) = 2.9$ were extracted from the fitting components, so the average valence of Eu was 2.15 under ambient conditions. The average Eu valence increased continuously as the pressure increased and reached a value of 2.5+ at 10.5 GPa, which was the highest pressure point measured (Figs. S1–S3). This value corresponds to an increase in the Eu valence of 0.35 during compression, which is comparable to the pressure-induced changes reported for the Eu-containing compound $EuMnBi_2$, i.e., an increase in the Eu valence of 0.4 under pressure applied at 25 GPa [30].

3.4. High pressure synchrotron PXRD measurements

In order to understand the correlations between the valence states of the Eu ion and the structural evolution of $CsEuF_3$ under pressure, we conducted an in-situ high pressure synchrotron PXRD experiment at room temperature up to 23 GPa. Selected synchrotron PXRD profiles obtained at various pressure points are shown in Fig. 6, and the unit cell metrics across all pressures were assessed using the Le Bail algorithm. The diffraction data sets collected as the pressure increased indicated that no structural changes occurred up to 6.0 GPa, with monotonic decreases in the lattice constants and unit-cell volume. Above 7.0 GPa, the sample underwent a first-order phase transition from a cubic to tetragonal unit cell, where the profile was best indexed by space group P4/

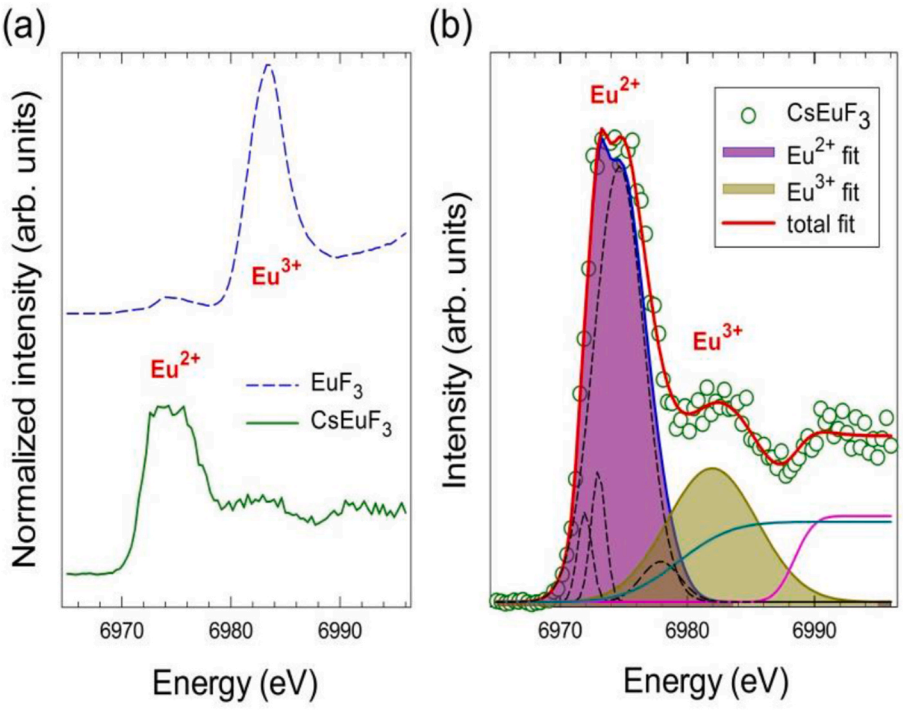

Fig. 4. (a) HERFD-XAS spectra recorded at the Eu-L_3 edge for $CsEuF_3$ (solid green line) at ambient conditions and for EuF_3 (dashed blue line) as a reference. (b) Representative fit (solid red line through the data) of the experimental data (open circle) for $CsEuF_3$. The two main peaks for the Eu^{2+} and Eu^{3+} states are represented as purple and dark yellow shaded areas, respectively. The arctangent functions used to characterize the background for the continuum transitions are represented by two solid lines in cyan and pink.

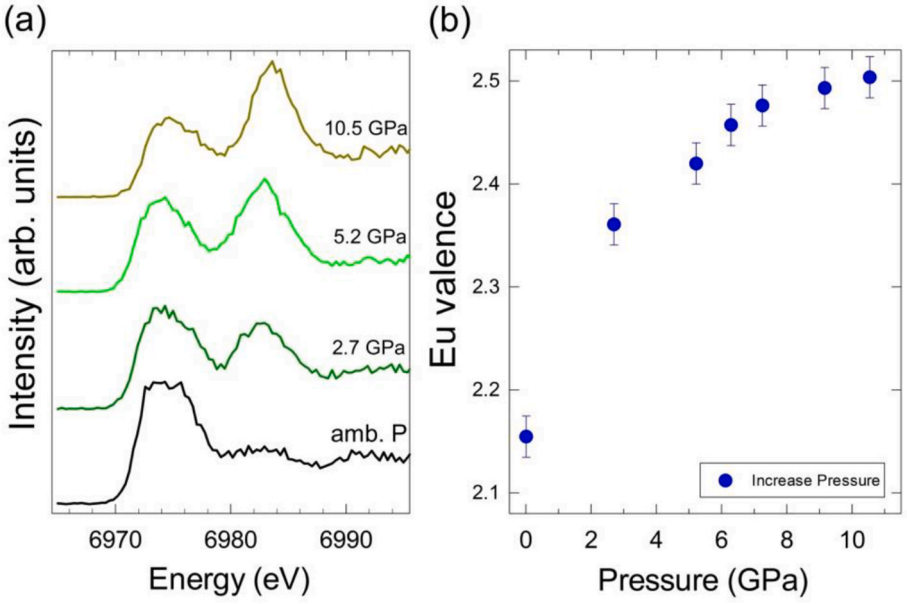

Fig. 5. (a) Room temperature Eu L_3-edge HERD-XAS spectra obtained for $CsEuF_3$ as the pressure increased. (b) Average valence of Eu as a function of pressure.

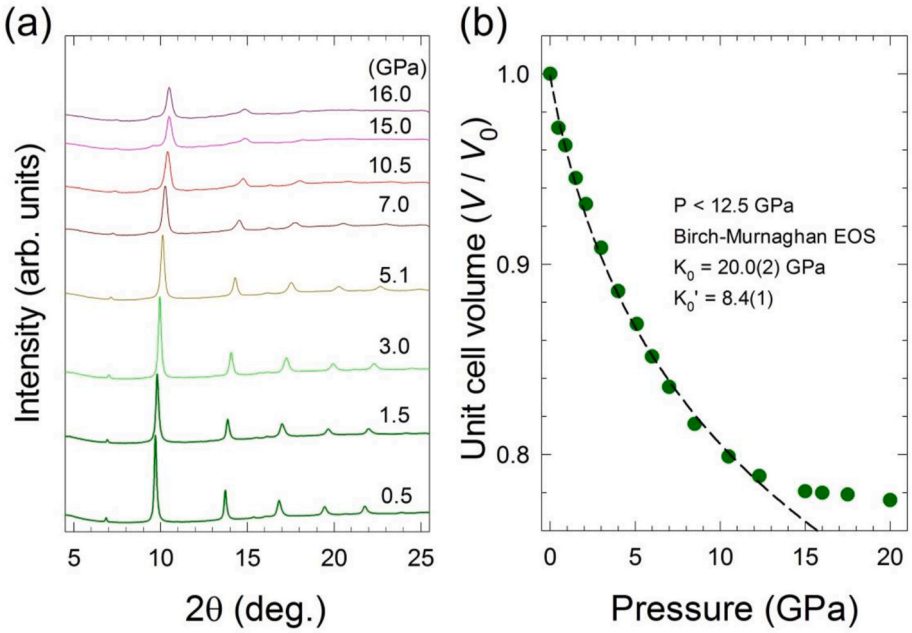

Fig. 6. (a) Selected room temperature synchrotron PXRD profile ($\lambda = 0.5657$ Å) for $CsEuF_3$ phase obtained under compression from 0.5 to 23.0 GPa. (b) Derived unit cell volume as a function of pressure. The dashed line through the data points represents the least-squares fit to the Birch–Murnaghan equation of state for the data points below 12 GPa.

mbm (Figs. S4 and S5). Depressurization from 10.5 GPa to 0.01 GPa led to recovery of the low pressure cubic phase, thereby suggesting that the cubic to tetragonal phase transition is reversible. No further phase transition occurred after increasing the pressure above 7.0 GPa but the lattice constants continued to contract up to 18.0 GPa. When the sample was compressed above 23.0 GPa, the diffraction peaks broadened rapidly and the sample began to decompose, and the cubic phase could no longer be recovered even after all of the applied pressure was released. Fig. 6b shows the evolution of the $CsEuF_3$ unit cell volume under pressure and the least-squares fit of the equation of state to the semiempirical third-order Birch–Murnaghan equation. After accounting for the V(P) data up to 12.0 GPa, the fit yielded an atmospheric pressure isothermal bulk modulus of $K_0 = 20.0(2)$ GPa and a pressure derivative of $K_{0'} = 8.4$. The calculated value of K_0 implies that $CsEuF_3$ exhibits significantly higher compressibility than other fluoroperovskites that do not contain Eu, such as $K_0 = 54.8$ GPa for $KZnF_3$ [31] and 65.8 GPa for $NaNiF_3$ [32]. The smaller bulk modulus of Eu-containing compounds under pressure is expected because the Eu^{3+} ion has a smaller ionic radius than Eu^{2+}, and the pressure-induced valence transition from Eu^{2+} to Eu^{3+} resulted in a rapid contraction in volume by 20% at 10.0 GPa and total contraction by 22% at 20.0 GPa.

4. Discussion

Valence instability in RE-based systems in response to changes in external stimuli, such as temperature or pressure (chemical or physical),

is relatively rare but it can be observed in RE elements, intermetallic alloys, and compounds [33,34]. This type of transition can occur in materials containing "anomalous" RE elements, such as Ce, Yb, Eu, Sm, or Tm. The chemistry of these elements can exist in tetravalent or divalent oxidation states in addition to the predominant trivalent state. To the best of our knowledge, $CsEuF_3$ is the first example of a RE fluorite material with a perovskite structure that exhibits external stimuli-dependent valence transitions.

Macroscopic property measurements such as magnetic susceptibility measurements are useful for studying valence instabilities in anomalous RE-based systems because valence fluctuations can occur between a magnetic state and non-magnetic valence state.

Recently, temperature and pressure induced valence transitions in Eu-based materials were studied in materials such as $Eu_2Pt_6Al_{15}$, $EuMnBi_2$, and $EuRh_2Si_2$. These studies were based on magnetic susceptibility measurements, XAS, hard X-ray photoelectron spectroscopy, and Mössbauer spectroscopy [30,35–37]. All of these studies provided detailed observations related to the electronic structure of the RE element and they showed that the origin of valence transitions can be explained by the single-impurity Anderson model. Theoretical analyses based on the Anderson model predict that the change in valence state is due to changes in the energy levels of the trivalent Eu multiplet because of changes in the hybridization of 4*f* electrons with the conduction band electrons. Similarly, the temperature and pressure induced valence transitions in $CsEuF_3$ can be attributed to the change in the *f-d* hybridization strength and the overlap of the d-states with the anion orbitals. Additional temperature-dependent multiple X-ray spectroscopy investigations are currently being conducted in our laboratories to obtain further insights into the origin of the transition in this system.

The application of physical and/or chemical pressure to these systems is a promising direction for further research because it allows for finer tuning to higher average valences, which are necessary for the transition of $CsEuF_3$ from an insulator to a metal under high pressure. For example, it was shown that the application of physical pressure on $EuRh_2Si_2$ increased the maximum average valence change by 15% [36,37]. Another example is the effect of chemical pressure yielding SmS and $Sm_{2.75}C_{60}$ [38,39] due to co-intercalation of the valence precise Ca^{2+} ion, which can cause valence fluctuation under ambient conditions.

5. Conclusions

In this study, we synthesized a polycrystalline cubic $CsEuF_3$ perovskite compound and investigated its electronic and structural changes under applied pressure. HERFD-XAS measurements at ambient conditions showed that the Eu ion is in the divalent oxidation state. This is consistent with the effective magnetic moment of 7.62 μ_B per Eu ion indicated by the inverse magnetic susceptibility. In addition, when the temperature was lowered to 1.8 K, the effective magnetic moment dropped rapidly to 6.07 μ_B per Eu ion, thereby indicating the conversion of 24% of the Eu^{2+} to Eu^{3+}, which we interpreted as a sign of strong *f-d* hybridization in the system. Applying hydrostatic pressure up to 10.5 GPa increased the valence transition and 50% of the Eu^{2+} converted into Eu^{3+}.

Funding

This work was financially supported by the National Key Research and Development Program of China (2018YFA0305703), Science Challenge Project (No. TZ2016001), and National Natural Science Foundation of China (NSFC: U1930401, 11874075).

Sample availability

A sample of $CsEuF_3$ powder is available from T.N. (takeshi.nakagawa@hpstar.ac.cn).

Author statement

Takeshi Nakagawa: Conceptualization, sample synthesis, carry out experiments, data analysis, original draft preparation, **Martina Vrankić:** formal XRD data analysis, **Melita Menelaou:** review and editing, **Raimundas Sereika:** participation in experiment, **Dong Wang:** sample preparation, **Jianbo Zhang:** experimental support, **Hirofumi Ishii:** experimental support, **Nozomu Hiraoka:** experimental support, **Yang Ding:** Supervision and funding acquisition, All authors have read and agreed to the published version of the manuscript.

Declaration of competing interest

The authors declare that they have no known competing financial interests or personal relationships that could have appeared to influence the work reported in this paper.

Data availability

Data will be made available on request.

Acknowledgments

We particularly thank Prof. K. Prassides for kindly providing us with the time to obtain X-ray diffraction and magnetic susceptibility data at Osaka Prefecture University. The experiments using the BL12B2 and BL12B2 at SPring-8 were performed under SPring-8 Proposal No. 2019A4132 and 2020A4260.

Appendix A. Supplementary data

Supplementary data to this article can be found online at https://doi.org/10.1016/j.jpcs.2022.111202.

References

[1] J. Arvanitidis, K. Papagelis, S. Margadonna, K. Prassides, A.N. Fitch, Temperature-induced valence transition and associated lattice collapse in samarium fulleride, Nature 425 (2003) 599–602, https://doi.org/10.1038/nature01994.
[2] S. Watanabe, K. Miyake, Quantum valence criticality as an origin of unconventional critical phenomena, Phys. Rev. Lett. 105 (2010), 186403, https://doi.org/10.1103/PhysRevLett.105.186403.
[3] B. Chen, E.M. Pärschke, W.-C. Chen, B. Scoggins, B. Li, M. Balasubramanian, S. Heald, J. Zhang, H. Deng, R. Sereika, Y. Sorb, X. Yin, Y. Bi, K. Jin, Q. Wu, C.-C. Chen, Y. Ding, H.-K. Mao, Probing cerium 4f states across the volume collapse transition by X-ray Raman scattering, J. Phys. Chem. Lett. 10 (2019) 7890–7897, https://doi.org/10.1021/acs.jpclett.9b02819.
[4] S. Danzenbächer, D.V. Vyalikh, Y. Kucherenko, A. Kade, C. Laubschat, N. Caroca-Canales, C. Krellner, C. Geibel, A.V. Fedorov, D.S. Dessau, R. Follath, W. Eberhardt, S.L. Molodtsov, Hybridization phenomena in nearly-half-filled f-shell electron systems: photoemission study of $EuNi_2P_2$, Phys. Rev. Lett. 102 (2009), 026403, https://doi.org/10.1103/PhysRevLett.102.026403.
[5] H.Q. Yuan, F.M. Grosche, M. Deppe, C. Geibel, G. Sparn, F. Steglich, Observation of two distinct superconducting phases in $CeCu_2Si_2$, Science 302 (2003) 2104–2107, https://doi.org/10.1126/science.1091648.
[6] M. Pazoki, T. Edvinsson, Metal replacement in perovskite solar cell materials: chemical bonding effects and optoelectronic properties, Sustain. Energy Fuels 2 (2018) 1430–1445, https://doi.org/10.1039/C8SE00143J.
[7] Z. Song, W. Xu, Y. Wu, S. Liu, W. Bi, X. Chen, H. Song, Incorporating of lanthanides ions into perovskite film for efficient and stable perovskite solar cells, Small 16 (2020), 2001770, https://doi.org/10.1002/smll.202001770.
[8] J.-P. Ma, Y.-M. Chen, L.-M. Zhang, S.-Q. Guo, J.-D. Liu, H. Li, B.-J. Ye, Z.-Y. Li, Y. Zhou, B.-B. Zhang, O.M. Bakr, J.-Y. Zhang, H.-T. Sun, Insights into the local structure of dopants, doping efficiency, and luminescence properties of lanthanide-doped $CsPbCl_3$ perovskite nanocrystals, J. Mater. Chem. C 7 (2019) 3037–3048, https://doi.org/10.1039/C9TC00237E.
[9] G. Pan, X. Bai, D. Yang, X. Chen, P. Jing, S. Qu, L. Zhang, D. Zhou, J. Zhu, W. Xu, B. Dong, H. Song, Doping lanthanide into perovskite nanocrystals: highly improved and expanded optical properties, Nano Lett. 17 (2017) 8005–8011, https://doi.org/10.1021/acs.nanolett.7b04575.
[10] W. Wang, Q. Meng, Y. Xue, X. Weng, P. Sun, Z. Wu, Lanthanide perovskite catalysts for oxidation of chloroaromatics: secondary pollution and modifications, J. Catal. 366 (2018) 213–222.
[11] L. Wang, K.A. Stoerzinger, L. Chang, J. Zhao, Y. Li, C.S. Tang, X. Yin, M.E. Bowden, Z. Yang, H. Guo, L. You, R. Guo, J. Wang, Tuning bifunctional oxygen

electrocatalysts by changing the A-site rare-earth element in perovskite nickelates, Adv. Funct. Mater. 28 (2018), 1803712, https://doi.org/10.1002/adfm.201803712.
[12] M.M. Lee, J. Teuscher, T. Miyasaka, T. Murakami, H.J. Snaith, Efficient hybrid solar cells based on meso-superstructured organometal halide perovskites, Science 338 (2012) 643–647, https://doi.org/10.1126/science.1228604.
[13] S. Margadonna, G. Karotsis, Cooperative Jahn-Teller distortion, phase transitions, and weak ferromagnetism in the $KCrF_3$ perovskite, J. Am. Chem. Soc. 128 (2006) 16436–16437, https://doi.org/10.1021/ja0669272.
[14] Z. Zeng, Y. Xu, Z. Zhang, Z. Gao, M. Luo, Z. Yin, C. Zhang, J. Xu, B. Huang, F. Luo, Y. Yaping Du, C. Yan, Rare-earth-containing perovskite nanomaterials: Design, synthesis, properties and applications, Chem. Soc. Rev. (2020), https://doi.org/10.1039/c9cs00330d.
[15] M.A. Carpenter, C.J. Howard, Symmetry rules and strain/order-parameter relationship for coupling between octahedral tilting and cooperative Jahn-Teller transitions in ABX_3 perovskites. I theory, Acta Crystallogr. B65 (2009) 134–146, https://doi.org/10.1107/S0108768109000974.
[16] R. Hoppe, G.-Q. Wu, Novel Fluoro Perovskites of Bivalent Lanthanoides. On $CsEuF_3$, $CsYbF_3$ und $RbYbF_3$, Z. Anorg. Allg. Chem. 504 (1983) 55–59, https://doi.org/10.1002/zaac.19835040907.
[17] G. Meyer, The synthesis and structure of complex rare-earth halides, Prog. Solid State Chem. 14 (1982) 141–219, https://doi.org/10.1016/0079-6786(82)90005-X.
[18] S. Hesse, J. Zimmermann, H. von Seggern, H. Ehrenber, H. Fuess, C. Fasel, R. Riedel, $CsEuBr_3$: crystal structure and its role in the photostimulation of CsBr: Eu^{2+}, J. Appl. Phys. 100 (2006), 083506 https://doi.org/10.1063/1.2358328.
[19] A. Jayaraman, V. Narayanamurti, E. Bucher, R.G. Maines, Continuous and discontinuous semiconductor-metal transition in samarium monochalcogenides under pressure, Phys. Rev. Lett. 25 (1970) 1430–1433, https://doi.org/10.1103/PhysRevLett.25.1430.
[20] P.S. Savchenkov, P.A. Alekseev, A. Podlesnyak, A.I. Kolesnikov, K.S. Nemkovski, Intermediate-valence state of the Sm and Eu in SmB_6 and $EuCu_2Si_2$: neutron spectroscopy data and analysis, J. Phys. Condens. Matter 30 (2018), 055801, https://doi.org/10.1088/1361-648X/aaa1aa.
[21] J. Kaštil, M. Míšek, J. Kamarád, Z. Arnold, K. Vlášková, J. Prchal, M. Diviš, P. Doležal, J. Prokleška, J. Valenta, J. Fikáček, A. Rudajevová, D. Kriegner, Properties of the divalent-Yb compound $YbAu_2Si_2$ under extreme conditions, Phys. B Condens. Matter 505 (2017) 41–44, https://doi.org/10.1016/j-physb.2016.10.030.
[22] B. Johansson, Energy position of 4f levels in rare-earth metals, Phys. Rev. B 20 (1979) 1315–1327, https://doi.org/10.1103/PhysRevB.20.1315.
[23] H.M. Rietveld, A profile refinement method for nuclear and magnetic structures, J. Appl. Crystallogr. 2 (1969) 65, https://doi.org/10.1107/S0021889869006558.
[24] R.J. Hill, C.J. Howard, Quantitative phase analysis from neutron powder diffraction data using the Rietveld method, J. Appl. Crystallogr. 20 (1987) 467–474, https://doi.org/10.1107/S0021889887086199.
[25] B.H. Tody, R.B. Von Dreele, GSAS-II: the genesis of a modern open-source all purpose crystallography software package, J. Appl. Crystallogr. 46 (2013) 544–549, https://doi.org/10.1107/S0021889813003531.
[26] E. Posnjak, R.W.G. Wyckoff, The crystal structures of the alkali halides, II J. Washington Acad. Sci. 12 (1922) 248–251.
[27] V.F. Zinchenko, N. Pefryushina, O. Geryomin, V. Yamarkiv, N. Mbelyavin, O. Vmozkova, M.I. Zakharenko, Synthesis, structure and optical properties of EuF3 film forming material, J. Alloys Compd. 347 (2002) 1–3, https://doi.org/10.1016/S0925-8388(02)00779-X.
[28] K. Hämäläinen, D.P. Siddons, J.B. Hasting, L.E. Berman, Elimination of the inner-shell lifetime broadening in X-ray absorption spectroscopy, Phys. Rev. Lett. 67 (1991) 2850, https://doi.org/10.1103/PhysRevLett.67.2850.
[29] H. Yamaoka, N. Tsujii, M.-T. Suzuki, Y. Yamamoto, I. Jarrige, H. Sato, J.-F. Lin, T. Mito, J. Mizuki, H. Sakurai, O. Sakai, N. Hiraoka, H. Ishii, K.-D. Tsuei, M. Giovannini, E. Bauer, Pressure-induced anomalous valence crossover in cubic $YbCu_5$-based compounds, Sci. Rep. 7 (2017) 5846, https://doi.org/10.1038/s41598-017-06190-3.
[30] R.A. Susilo, W. Deng, J. Feng, A. Wang, N. Kawamura, N. Ishimatsu, S. Kawaguchi, M. Yuan, H. Li, W. Ren, T. Nakagawa, C. Petrovic, B. Chen, Impacts of pressure to the structural, electronic and magnetic properties of Dirac semimetal $EuMnBi_2$, Phys. Rev. Res. 3 (2021), 043028, https://doi.org/10.1103/PhysRevResearch.3.043028.
[31] F. Aguado, F. Rodriguez, S. Hirai, J.N. Walsh, A. Lennie, S.A.T. Redfern, High-pressure behavior of KMF_3 perovskites, High Pres. Res.: Int. J. 28 (4) (2008) 539–544, https://doi.org/10.1080/08957950802576464.
[32] H. Yusa, Y. Shirako, M. Akaogi, H. Kojitani, N. Hirao, Y. Ohishi, T. Kikegawa, Perovskite-to-Postperovskite transitions in $NaNiF_3$ and $NaCoF_3$ and disproportionation of $NaCoF_3$ postperovskite under high pressure and high temperature, Inorg. Chem. 51 (2012) 6559–6566, https://doi.org/10.1021/ic300118d.
[33] B. Chen, M. Tian, J. Zhang, L. Bing, Y. Xiao, P. Chow, C. Kenney-Benson, H. Deng, J. Zhang, R. Sereika, X. Yin, D. Wang, X. Hong, C. Jin, Y. Bi, H. Liu, H. Liu, J. Li, K. Jin, Q. Wu, J. Chang, Y. Ding, H-k. Mao, Novel valence transition in elemental metal europium around 80 GPa, Phys. Rev. Lett. 129 (2022), 016401, https://doi.org/10.1103/PhysRevLett.129.016401.
[34] F. Stegemann, J. Stahl, M. Bartsch, H. Zacharias, D. Johrendt, O. Janka, Temperature induced valence phase transition in intermediate-valent $YbPd_2Al_3$, Chem. Sci. 10 (2019) 11086–11094, https://doi.org/10.1039/c9sc04437j.
[35] M. Radzieowski, F. Stegemann, T. Block, J. Stahl, D. Johrendt, O. Janka, Abrupt europium valence change in $Eu_2Pt_6Al_{15}$ around 45 K, J. Am. Chem. Soc. 140 (2018) 8950–8957, https://doi.org/10.1021/jacs.8b05188.
[36] A. Mitsuda, E. Kishaba, T. Fujimoto, K. Oyama, H. Wada, M. Mizumaki, N. Kawamura, N. Ishimatsu, Pressure and magnetic field effects on the valence transition of $EuRh_2Si_2$, Phys. B Condens. Matter 536 (2018) 427–431, https://doi.org/10.1016/j.physb.2017.10.045.
[37] A. Mitsuda, H. Wada, R. Masuda, S. Kitao, M. Seto, Y. Yoda, H. Kobayashi, Valence transition of $EuRh_2Si_2$ studied by synchrotron Mössbauer spectroscopy, J. Phys. Soc. Jpn. 89 (2020), 104703, https://doi.org/10.7566/JPSJ.89.104703.
[38] A. Jayaraman, R.G. Maines, Study of the valence transition in Eu-, Yb- and Ca-substituted SmS under high pressure and some comments on other substitutions, Phys. Rev. B 19 (1979) 4154–4161, https://doi.org/10.1103/PhysRevB.19.4154.
[39] N. Yoshikane, T. Nakagawa, K. Matsui, H. Yamaoka, N. Hiraoka, H. Ishii, J. Arvanitidis, K. Prassides, Chemical tuning of samarium valence in mixed valence $(Sm1_{-x}Ca_x)_{2.75}C_{60}$ fullerides, J. Phys. Chem. Solid. 150 (2020), 109822, https://doi.org/10.1016/j.jpcs.2020.109822.